Quantum-corrected drift-diffusion models: Solution fixed point map and finite element approximation

Carlo de Falco [a,1], Joseph W. Jerome [b,2], Riccardo Sacco [c,*,3]

[a] *School of Mathematical Sciences, Dublin City University, Glasnevin, Dublin 9, Ireland*
[b] *Department of Mathematics, Northwestern University, 2033 Sheridan Road, Evanston, IL 60208-2730, USA*
[c] *Dipartimento di Matematica "F.Brioschi", Politecnico di Milano, via Bonardi 9, 20133 Milano, Italy*

ARTICLE INFO

ABSTRACT

This article deals with the analysis of the functional iteration, denoted Generalized Gummel Map (GGM), proposed in [C. de Falco, A.L. Lacaita, E. Gatti, R. Sacco, Quantum-Corrected Drift-Diffusion Models for Transport in Semiconductor Devices, J. Comp. Phys. 204 (2) (2005) 533–561] for the decoupled solution of the Quantum Drift-Diffusion (QDD) model. The solution of the problem is characterized as being a fixed point of the GGM, which permits the establishment of a close link between the theoretical existence analysis and the implementation of a numerical tool, which was lacking in previous non-constructive proofs [N.B. Abdallah, A. Unterreiter, On the stationary quantum drift-diffusion model, Z. Angew. Math. Phys. 49 (1998) 251–275, R. Pinnau, A. Unterreiter, The stationary current–voltage characteristics of the quantum drift-diffusion model, SIAM J. Numer. Anal. 37 (1) (1999) 211–245]. The finite element approximation of the GGM is illustrated, and the main properties of the numerical fixed point map (discrete maximum principle and order of convergence) are discussed. Numerical results on realistic nanoscale devices are included to support the theoretical conclusions.

© 2008 Elsevier Inc. All rights reserved.

1. Introduction and motivation

The continuous advancement of the semiconductor industry makes it unavoidable to resort to numerical simulation to predict the electric properties of devices of the next generation well before their construction is actually feasible. In the current technology, the channel length of metal oxide semiconductor field effect transistors (MOSFETs) is of the order of tens of nanometers and the thickness of the oxide is of a few nanometers. Because of such small dimensions, quantum confinement and tunneling affect the performance of nanoscale devices in two main respects. First of all, quantization of energy states for electrons confined in the channel produces a shift of the charge peak, increasing the "equivalent oxide thickness" in such a way that the coupling of the gate and channel voltages is reduced. Secondly, the penetration of electrons under the channel barrier effectively smooths and lowers such barrier, increasing the off-state leakage current. To limit quantization effects, new device structures and geometries are investigated to overcome the traditional single-gate MOS transistor (see [36,10], Chapter 1). In any event, irrespective of the adopted device technology, it is a fact that, on the one hand, quantum

effects cannot be captured by a classical drift-diffusion (DD) description, and that, on the other hand, the "full quantum" models proposed in the literature (Wigner transport equation [16], non-equilibrium Green functions [9]) are, as of now, too costly to be adopted in industrial applications. This is the reason for the development of "quantum corrected drift-diffusion" (QCDD) models that are based on the introduction of a correction potential in the DD equation to account for quantum effects on the spatial distribution of charge carriers within the devices (see [3,32]). By adopting such models the computational complexity can be contained within reasonable limits at the cost of neglecting quantum effects on transport (coherent transport, interferences, reflections), which can be considered of higher order for devices of gate length higher than 10 nm [26].

In Refs. [11,10], a general mathematical framework for QCDD models has been proposed and subjected to extensive investigation in the numerical study of advanced nanoscale MOSFET and double-gate (DG) MOSFET devices. One of the main contributions of the cited references consists of the introduction of a fixed point map, named generalized Gummel map (GGM), for the iterative solution of the nonlinearly coupled system of model equations. The GGM is the natural extension to the quantum-corrected setting of the Gummel's decoupled algorithm traditionally used in DD simulation [15,27,19], and has two significant benefits. The first benefit is to maintain the *same* functional structure irrespective of the *specific* choice of the quantum-corrected model. The second benefit, which applies to the particular case of the quantum DD (QDD) model, the object of this article, is to provide an *effective* computational tool for the numerical solution of the variational formulation proposed in Refs. [1,31] to treat the quantum correction to the DD system. In the present article, we intend to characterize the solution of the QDD transport model as being a fixed point of the GGM. This establishes a close link between the theoretical existence analysis and the implementation of a numerical tool which was lacking in previous non-constructive proofs (cf. [1,31]). The principal instruments used to demonstrate the existence of a fixed point of the GGM are (i) the introduction of a truncation operator, to prevent the occurrence of singularities in the quantum corrections, as proposed in Ref. [1]; (ii) the extension of the theory of invariant regions, used in [19] in the DD case, to the case of systems of nonlinear reaction–diffusion partial differential equations (PDEs) in non-gradient form; and (iii) a homotopy method based on the general theory developed in [17] to select the solution of each equation yielding the quantum corrections, for which uniqueness is not guaranteed due to the lack of monotonicity of the semi-linear terms. Once the existence of a fixed point of the map is proved, the finite element approximation of the GGM is worked out along the same lines as in the classical DD setting, ending up with discrete maximum principles and optimal order of convergence.

A brief outline of the article is as follows. In Section 2, we introduce the QDD model and the associated scaling and modeling parameters. In Section 3 we illustrate the GGM for the iterative solution of the QDD model, and address some computational remarks on the structure of the algorithm in Section 4. The analysis of existence of a fixed point of the GGM is carried out in Section 5, while in Section 6 we illustrate the discretized model and the numerical counterpart of the GGM. In Section 7, we conduct a series of numerical experiments to demonstrate the validity of the GGM applied to the simulation of realistic nanoscale devices, while in Section 8 we draw some conclusions and future work perspectives. In Appendices A, B and C we illustrate the main theoretical properties and instruments needed to extend the theory of invariant regions to the treatment of the QDD model.

2. The quantum drift-diffusion model

Under isothermal and steady-state regimes, the quantum drift-diffusion (QDD) model for nanoscale semiconductor device simulation can be written in the following dimensionless form [2,21]:

$$
\begin{cases}
-\mathrm{div}(\lambda^2 \mathbf{V}\varphi) = p - n + D, \\
-\delta_n^2 \Delta\sqrt{n} + \sqrt{n}(\varphi_n - \varphi + \ln(n)) = 0, \\
\quad G_n = \varphi_n - \varphi + \ln(n), \\
-\delta_p^2 \Delta\sqrt{p} + \sqrt{p}(-\varphi_p + \varphi + \ln(p)) = 0, \\
\quad G_p = \varphi_p - \varphi - \ln(p), \\
-\mathrm{div}(\mu_n(\mathbf{V}n - n\mathbf{V}(\varphi + G_n))) = -U, \\
-\mathrm{div}(\mu_p(\mathbf{V}p + p\mathbf{V}(\varphi + G_p))) = -U.
\end{cases}
\tag{1}
$$

The structure of (1), comprising algebraic and partial differential equations, matches closely the fixed point map that is adopted for its iterative solution, and qualifies the QDD model as a special member of the family of quantum-corrected DD (QCDD) models presented and extensively validated in [11]. In detail, $(1)_1$ is the Poisson equation for the electrostatic potential φ, $(1)_6$–$(1)_7$ are the carrier continuity equations for the electron and hole carrier concentrations n and p, while $(1)_2$–$(1)_3$ and $(1)_4$–$(1)_5$ provide a self-consistent definition of the quantum corrections G_n and G_p as functions of φ, n, p and the quantum quasi–Fermi potentials φ_n and φ_p. Inverting $(1)_3$ and $(1)_5$ yields the generalized Maxwell–Boltzmann statistics

$$
n = \exp((\varphi + G_n) - \varphi_n), \quad p = \exp(\varphi_p - (\varphi + G_p)).
\tag{2}
$$

System (1) is to be solved in a polyhedral semiconductor device domain $\Omega \subset \mathbb{R}^d$, $d = 1, 2, 3$, with boundary $\Gamma = \Gamma_D \cup \Gamma_N \cup \Gamma_A$ and outward unit normal vector $\mathbf{n}$, having set $\Gamma_D = \Gamma_+ \cup \Gamma_0$. The pairwise disjoint partitions of Γ_+ and Γ_0 physically
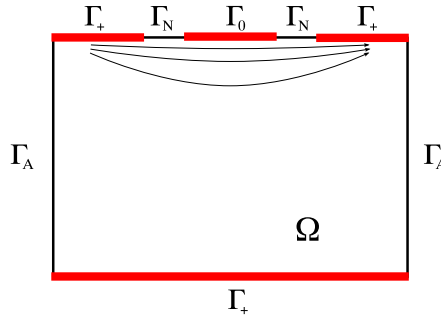
Fig. 1. Two-dimensional cross-section of the semiconductor device.

represent the ohmic contacts and material interfaces, while Γ_N and Γ_A physically represent the portions of the boundary separating the device domain from the external environment and neighboring devices. Boundary conditions for system (1) are enforced as follows:

$$\begin{cases} \varphi = \varphi_D, & n = n_D, \quad p = p_D \quad \text{on } \Gamma_+, \\ \varphi = \varphi_D, & n = p = 0 \qquad \text{on } \Gamma_0, \\ \nabla\varphi \cdot \mathbf{n} = \mathbf{J}_n \cdot \mathbf{n} = \mathbf{J}_p \cdot \mathbf{n} = 0 \quad \text{on } \Gamma_N, \end{cases} \tag{3}$$

having defined the current densities $\mathbf{J}_n = \mu_n(\nabla n - n\nabla(\varphi + G_n))$ and $\mathbf{J}_p = -\mu_p(\nabla p + p\nabla(\varphi + G_p))$. The boundary data φ_D, n_D and p_D are computed assuming charge neutrality and thermal equilibrium on Γ_+, while on Γ_0 the prescribed value of φ_D is the external voltage applied at the gate contact up to the voltage drop across the gate oxide layer. Our choice of the geometry and of the boundary conditions is a rather crude simplification of a MOSFET, because Ω does not comprise the oxide buffer region that is located over the interface Γ_0, and a two-dimensional example is depicted in Fig. 1. It is worth noting, however, that the iterative solution map proposed in this work can be readily extended to deal also with the case where the oxide region is included in the simulation domain, as documented by the numerical experiments discussed in Section 7 and in Ref. [11]. Some remarks are in order about the scaling and modeling parameters in (1). The quantities λ, δ_n and δ_p are positive singular perturbation parameters resulting from the application of a scaling procedure [11]. Setting $\delta_n = \delta_p = 0$, which corresponds to formally performing the classical limit $\hbar \to 0$, allows the recovery of the standard DD model. We refer to [11, Section 2.4], for the explicit expressions of the parameters and of their numerical values. The quantity D is a given function and represents the doping profile of the device. We assume that $D \in L^\infty(\Omega)$, with $D_{\min} = \inf_\Omega D$ and $D_{\max} = \sup_\Omega D$, where the operators $\inf_\Omega$ and $\sup_\Omega$ denote the essential infimum and the essential supremum in Ω, respectively. The quantities μ_n and μ_p are the carrier mobilities, and depend in a quite complex manner on the problem unknowns and on several other physical parameters, as extensively discussed in [35, Chapter 4]. We assume that $\mu_v, v = n, p$ are strictly positive bounded functions, referring to [19, Section 4.2], for a precise characterization of the polynomial decay of μ_v at the transition points of Γ. The quantity U is the net recombination rate, and accounts for recombination (R) and generation (G) effects in the semiconductor material. Several models for U are proposed in the literature to describe R/G effects in a quantum-modified setting (see [1,4]). As the impact of R/G phenomena is not very relevant for the class of applications we target in the numerical simulations of Section 7, in the following we will assume, for sake of simplicity, that $U = 0$. The extension of the proposed iterative solution map to cover also the case where $U \neq 0$ can be carried out by properly adapting the "lagging" procedure proposed for the DD model in Section 4.4 of [19] and for the QDD model in Section 2.3 of [1].

3. The generalized Gummel map

In this section, we illustrate the fixed point map for the iterative solution of the QDD model (1). The method, proposed and extensively validated in Refs. [11,10], is a consistent generalization of the classical Gummel map used in the decoupled treatment of the DD equations [19], and for this reason it is henceforth denoted as *Generalized Gummel Map* (GGM). Compared to the approach of Ref. [1], the GGM proposed in the present article exhibits two main differences. The first difference is that the GGM, unlike the maps of [1,31], embodies in a natural way a numerical algorithm suitable for implementation. In particular, the variational formulation used in Refs. [1,31] to deal with the coupled subsystem comprising Eqs. $(1)_1$–$(1)_5$, is replaced in the GGM by a fixed point iteration (Inner Loop) which is the extension to the quantum-corrected setting of the nonlinear iteration on the Poisson's equation $(1)_1$ that is usually carried out in the DD setting. The second difference is in the method used to enforce uniform ellipticity in the treatment of the carrier continuity equations. In Refs. [1,31], these latter equations are solved for the quantum quasi-Fermi potentials, and a proper truncation of the densities is used to ensure the strict positivity of the diffusion coefficient. In the present approach, the continuity equations are solved for the Slotboom variables as in standard DD theory [19], and the strict positivity of the diffusion coefficient is imposed by truncating the quantum corrections due to the Bohm potentials.

3.1. Preliminaries

Proceeding as in the case of the DD model (cf. [19], Section 4.3), we define the following constants:

$$\alpha = \min(\inf_{\Gamma_+} \varphi_n, \inf_{\Gamma_+} \varphi_p) = \inf_{\Gamma_+} \varphi_a + \ln(\theta),$$
$$\beta = \max(\sup_{\Gamma_+} \varphi_n, \sup_{\Gamma_+} \varphi_p) = \sup_{\Gamma_+} \varphi_a - \ln(\theta),$$

where φ_a is the externally applied bias and $\theta := n_{int}/\bar{n}$, n_{int} and $\bar{n}$ denoting the intrinsic concentration in the semiconductor material and the scaling factor for carrier concentrations, respectively. For the purpose of the analysis of the existence of a fixed point of the GGM, the above quantities should provide the upper and lower bounds for the invariant region to which the fixed point belongs. With this aim, it is useful to *symmetrize* the bounding interval $[\alpha, \beta]$ by introducing, as in Ref. [1], the following constants:

$$m = -\|\varphi_a\|_{L^\infty(\Gamma_+)} + \ln(\theta) - 1 \leqslant \alpha, \quad M = -m = \|\varphi_a\|_{L^\infty(\Gamma_+)} - \ln(\theta) + 1 \geqslant \beta,$$

with $m \leqslant 0$ and $M \geqslant 0$. For any nonnegative carrier concentrations n and p, we set $w := n^{1/2}$ and $z := p^{1/2}$, and for any bounded potential φ, we define the auxiliary variables

$$\sigma_n(w, \varphi) := w^2 e^{-\varphi}, \quad \sigma_p(z, \varphi) := z^2 e^{\varphi}. \tag{4}$$

For any bounded quantum quasi-Fermi potentials φ_n and φ_p, we introduce the quantum Slotboom variables

$$\rho := \exp(-\varphi_n), \quad \omega := \exp(\varphi_p), \tag{5}$$

in such a way that the generalized Maxwell–Boltzmann statistics (2) can be written in the equivalent form

$$n = \rho \exp(\varphi + G_n), \quad p = \omega \exp(-(\varphi + G_p)). \tag{6}$$

Then, we define the closed convex set

$$K = \{[v, w] \in (L^2(\Omega) \times L^2(\Omega)) : m \leqslant v(x), w(x) \leqslant M, \text{ a.e. in } \Omega\}, \tag{7}$$

and for any function g and any fixed $\delta \in (0, 1]$, we introduce the *truncation operator*

$$[g]_\delta := \max(g, \delta).$$

We also let $\mathcal{V} := H^1(\Omega) \cap L^\infty(\Omega)$.

3.2. The outer iteration loop

Given a pair $[\tilde{\varphi}_n, \tilde{\varphi}_p] \in K$, and $\delta \in (0, 1]$, the GGM for the iterative solution of the QDD system (1) consists of the following steps (*Outer Loop*):

Step 1: Use the fixed point iteration described in Section 3.3 to solve in the domain Ω the nonlinear system:

$$\begin{cases} -\mathrm{div}(\lambda^2 \mathbf{V}\varphi_\delta) + w_\delta^2 - z_\delta^2 - D = 0, \\ -\delta_n^2 \Delta w_\delta + w_\delta(\tilde{\varphi}_n - \varphi_\delta + 2\ln([w_\delta]_\delta)) = 0, \\ -\delta_p^2 \Delta z_\delta - z_\delta(\tilde{\varphi}_p - \varphi_\delta - 2\ln([z_\delta]_\delta)) = 0, \end{cases} \tag{8}$$

subject to the boundary conditions:

$$\begin{cases} \varphi_\delta = \varphi_D \quad \text{on } \Gamma_D, \quad \mathbf{V}\varphi_\delta \cdot \mathbf{n} = 0 \quad \text{on } \Gamma_N, \\ w_\delta = n_D^{1/2} \quad \text{on } \Gamma_+, \quad w_\delta = 0 \quad \text{on } \Gamma_0, \qquad \nabla w_\delta \cdot \mathbf{n} = 0 \quad \text{on } \Gamma_N, \\ z_\delta = p_D^{1/2} \quad \text{on } \Gamma_+, \quad z_\delta = 0 \quad \text{on } \Gamma_0, \qquad \nabla z_\delta \cdot \mathbf{n} = 0 \quad \text{on } \Gamma_N. \end{cases} \tag{9}$$

Step 2: Define the regularized quantum corrections:

$$G_{n_\delta} = \tilde{\varphi}_n - \varphi_\delta + 2\ln([w_\delta]_\delta), \quad G_{p_\delta} = \tilde{\varphi}_p - \varphi_\delta - 2\ln([z_\delta]_\delta), \tag{10}$$

and the quantum-corrected potentials

$$V_{n_\delta} := \varphi_\delta + G_{n_\delta}, \quad V_{p_\delta} := \varphi_\delta + G_{p_\delta}. \tag{11}$$

Step 3: Solve in the domain Ω the linear, uncoupled continuity equations:

$$-\mathrm{div}(\mu_n e^{V_{n_\delta}} \mathbf{V}\rho_\delta) = 0, \tag{12}$$
$$-\mathrm{div}(\mu_p e^{-V_{p_\delta}} \mathbf{V}\omega_\delta) = 0, \tag{13}$$

subject to the boundary conditions:

$$\begin{cases} \rho_\delta = \rho_D & \text{on } \Gamma_+, \quad \nabla\rho_\delta \cdot \mathbf{n} = 0 \quad \text{on } \Gamma_0 \cup \Gamma_N, \\ \omega_\delta = \omega_D & \text{on } \Gamma_+, \quad \nabla\omega_\delta \cdot \mathbf{n} = 0 \quad \text{on } \Gamma_0 \cup \Gamma_N. \end{cases} \tag{14}$$

Step 4: Update the quantum quasi-Fermi potentials by inverting (5):

$$\varphi_n = -\ln(\rho_\delta), \quad \varphi_p = \ln(\omega_\delta). \tag{15}$$

3.3. The inner iteration loop

Given $[\widehat{\varphi}_\delta, \widehat{w}_\delta, \widehat{z}_\delta] \in (\mathcal{V})^3$ and satisfying the essential boundary conditions in (9), with $\widehat{w}_\delta \geqslant 0$ in Ω and $\widehat{z}_\delta \geqslant 0$ in Ω, the inner loop for the solution of the nonlinear system (8) consists of the following steps:

Step A: Solve the nonlinear Poisson equation for the updated potential φ_δ:

$$\begin{cases} -\text{div}(\lambda^2 \nabla\varphi_\delta) + \sigma_{n,\delta}(\widehat{w}_\delta, \widehat{\varphi}_\delta)e^{\varphi_\delta} - \sigma_{p,\delta}(\widehat{z}_\delta, \widehat{\varphi}_\delta)e^{-\varphi_\delta} - D = 0, & \text{in } \Omega \\ \varphi_\delta = \varphi_D & \text{on } \Gamma_D, \\ \nabla\varphi_\delta \cdot \mathbf{n} = 0 & \text{on } \Gamma_N. \end{cases} \tag{16}$$

Step B: Solve the nonlinear Bohm equation for the updated square root of the electron concentration w_δ:

$$\begin{cases} -\delta_n^2 \Delta w_\delta + w_\delta(\tilde{\varphi}_n - \varphi_\delta + 2\ln([w_\delta]_\delta)) = 0, & \text{in } \Omega, \\ w_\delta = n_D^{1/2} & \text{on } \Gamma_+, \\ w_\delta = 0 & \text{on } \Gamma_0, \\ \nabla w_\delta \cdot \mathbf{n} = 0 & \text{on } \Gamma_N. \end{cases} \tag{17}$$

Step C: Solve the nonlinear Bohm equation for the updated square root of the hole concentration z_δ:

$$\begin{cases} -\delta_p^2 \Delta z_\delta - z_\delta(\tilde{\varphi}_p - \varphi_\delta - 2\ln([z_\delta]_\delta)) = 0, & \text{in } \Omega, \\ z_\delta = p_D^{1/2} & \text{on } \Gamma_+, \\ z_\delta = 0 & \text{on } \Gamma_0, \\ \nabla z_\delta \cdot \mathbf{n} = 0 & \text{on } \Gamma_N. \end{cases} \tag{18}$$

3.4. Abstract formulation of the GGM

The outer iteration loop described in Section 3.2 can be interpreted as the application of the fixed point map $\mathbf{T} : K \to K$ to a given pair $[\tilde{\varphi}_n, \tilde{\varphi}_p]$, in such a way that the following relation holds

$$[\varphi_n, \varphi_p] = \mathbf{T}(\tilde{\varphi}_n, \tilde{\varphi}_p). \tag{19}$$

To characterize in detail the action of $\mathbf{T}$, we need to introduce the operators that represent the various steps of the solution map. For a given $\delta \in (0, 1]$, we denote by $\mathbf{U} : K \to (\mathcal{V})^3$ the operator associating with $[\tilde{\varphi}_n, \tilde{\varphi}_p]$ the triple $[\varphi_\delta, [w_\delta]_\delta, [z_\delta]_\delta]$ through the solution of (8) as described in Section 3.3. Then, we denote by $\mathbf{V}_n : (L^\infty(\Omega))^3 \to L^\infty(\Omega)$ and $\mathbf{V}_p : (L^\infty(\Omega))^3 \to L^\infty(\Omega)$ the
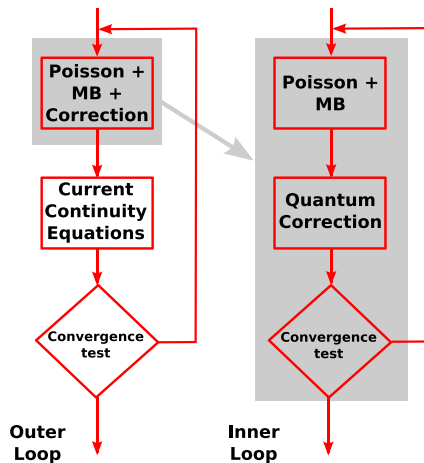

Fig. 2. A flow-chart of the GGM.

operators associating with the triples $[\varphi_\delta, \tilde{\varphi}_n, [w_\delta]_\delta]$ and $[\varphi_\delta, \tilde{\varphi}_p, [z_\delta]_\delta]$ the bounded functions V_{n_δ} and V_{p_δ} through the combined use of (10) and (11). Finally, we denote by $\mathbf{R} : L^\infty(\Omega) \rightarrow \mathcal{V}$ and $\mathbf{W} : L^\infty(\Omega) \rightarrow \mathcal{V}$ the operators associating with V_{n_δ} and V_{p_δ} the solutions of the linear continuity subproblems (12)–(14)$_1$ and (13) and (14)$_2$. The composition of the action of the above operators yields the following definition of the fixed point operator associated with the GGM

$$\mathbf{T} := [-\ln \mathbf{R} \circ \mathbf{V}_n \circ \mathbf{U}, \ln \mathbf{W} \circ \mathbf{V}_p \circ \mathbf{U}]. \tag{20}$$

It is interesting to notice that this definition generalizes to the quantum-corrected setting the standard framework valid in the case of the DD model, because in this latter case $\mathbf{V}_n$ and $\mathbf{V}_p$ coincide with the identity operator [20]. A flow-chart of the GGM is depicted in Fig. 2.

4. Computational remarks on the GGM

We collect below some computational remarks on the various steps of the fixed point map introduced in Sections 3.2 and 3.3.

Let us start from the outer iteration loop.

4.1. Step 1

(1) It is shown in Ref. [1] (cf. Theorem 2.1) that problem (8) and (9) admits a unique solution $[w_\delta, z_\delta, \varphi_\delta = \varphi_\delta(w_\delta, z_\delta)] \in (\mathcal{V})^3$ satisfying the a priori estimates

$$\|w_\delta\|_{L^\infty(\Omega)}, \|w_\delta\|_{H^1(\Omega)}, \|z_\delta\|_{L^\infty(\Omega)}, \|z_\delta\|_{H^1(\Omega)} \leqslant \mathcal{K}, \tag{21}$$

where $\mathcal{K} = \mathcal{K}(M)$ is a positive constant *not* depending on δ.
(2) The same structure of Step 1 is maintained if the QDD model is replaced by other different quantum-corrected models (cf. Ref. [11], Sections 4 and 6).

4.2. Step 2

The introduction of the truncation operator $[\cdot]_\delta$ prevents the occurrence of singularities in the quantum-corrected potentials introduced in (11). As a matter of fact, the numerical experiments of Section 7 show that the Bohm potentials G_{n_δ} and G_{p_δ} are *bounded inside the device domain independently of the chosen value of* δ, and become unbounded *only* at the inversion layer contact Γ_0, consistently with the physical fact that, in the quantum-modified description, the carrier densities are exactly set equal to zero at Γ_0. This confirms the validity of (21) and agrees also with the conclusions drawn from the simulations reported in Ref. [11].

4.3. Step 3

Using (6) and noting that $G_{n,\delta} = G_{p,\delta} = 0$ on Γ_+, the boundary data ρ_D and ω_D can be computed as $\rho_D = n_D \exp(-\varphi_D) = \theta \exp(-\varphi_a|_{\Gamma_+})$, $\omega_D = p_D \exp(\varphi_D) = \theta \exp(\varphi_a|_{\Gamma_+})$. Then, using Lemma 3.2.2 [27], it can be shown that BVPs (12)–(14)$_1$ and (13) and (14)$_2$ admit a unique solution pair $[\rho_\delta, \omega_\delta] \in (\mathcal{V})^2$ satisfying the essential boundary conditions in (14) and the maximum principles

$$e^{-M} \leqslant \rho_\delta(x) \leqslant e^M, \quad e^{-M} \leqslant \omega_\delta(x) \leqslant e^M \quad \text{a.e.in } \Omega. \tag{22}$$

Let us now consider the inner iteration loop.

(1) The inner loop is a *consistent generalization* to the QCDD setting of the nonlinear iteration that is usually carried out in the DD setting, and *provides a constructive computational approach* to the variational formulation used in [1,31].
(2) System (16)–(18) is based on the combined use of the generalized Maxwell–Boltzmann statistics (6) and of the Gauss–Seidel method in the nonlinear system (8). As a matter of fact, the Poisson Eq. (16) is nonlinear with respect to φ_δ, unlike the linear counterpart (8)$_1$. This is the price to be paid for introducing an inner decoupling in system (8).
(3) Each nonlinear problem in (16)–(18) is solved by resorting to a properly damped Newton's method and the numerical approximation of the corresponding sequence of iterates is carried out by the Galerkin finite element method (see [11], Section 5.1).
(4) A careful selection of the damping parameter in the linearization of the Bohm potential Eqs. (17) and (18) introduces a parabolic regularization which ensures that a discrete maximum principle holds for the approximate solutions $w_{\delta,h}$ and $z_{\delta,h}$. This, in turn, implies that

$$w_{\delta,h}(x) > 0 \text{ and } z_{\delta,h}(x) > 0 \quad \forall x \in \Omega.$$

(5) Extensive numerical experiments carried out in [11] show that convergence of the inner loop may be slowed down by the introduction of the damping strategy, especially in presence of significant quantum corrections at the inversion layer boundary Γ_0. In such a case, the use of vectorial acceleration algorithms gives rise to a substantial reduction of the computational cost associated with the GGM iteration (see [10]).

5. Existence analysis of a fixed point of the GGM

In this section, we address the issue of well-posedness of the various iteration steps of the GGM and we prove the existence of a fixed point of the map.

5.1. Well-posedness of the outer iteration

The well-posedness of the outer iteration described in Section 3.2 is based upon the fixed point analysis of Ben-Abdallah and Unterreiter [1]. For fixed $\delta \in (0, 1]$, step 1 adopts the system arising as the Euler–Lagrange equations associated with the *functional minimization procedure* of [1], while steps 2, 3 and 4 are *equivalent* to the completion of the definition of the fixed point mapping T_δ of [1]. Subsequent analysis in [1] demonstrates convergence as $\delta \to 0$. In Ref. [1], it is shown that for each fixed $\delta \in (0, 1]$:

(i) The outer loop *has a fixed point pair*, defined by the pair of quantum quasi-Fermi levels φ_n, φ_p (cf. (15)).
(ii) There exist (non-constructive) bounds *independent of* δ for the functions w_δ and z_δ (cf. (21)). This implies that φ_δ can be bounded independently of δ because of the unique solvability of (8)$_1$ for given w_δ and z_δ, and the same holds also for the auxiliary variables $\sigma_{n,\delta}, \sigma_{p,\delta}$ defined in (4), for which we have the following 'a priori' positive bounds

$$0 \leqslant \sigma_{n,\delta}(x) \leqslant \beta_n, \quad 0 \leqslant \sigma_{p,\delta}(x) \leqslant \beta_p \quad \forall x \in \Omega, \tag{23}$$

where β_n and β_p are positive constants depending on $\mathcal{K}$ but *independent of* δ.

The 'a priori' estimates (23) permit the *definition of invariant regions* for the composition mappings associated with the inner iteration loop. This is the object of the following section.

5.2. Well-posedness of the inner iteration: 'A Priori' bounds and invariant regions

As defined, the inner loop proceeds by first solving the nonlinear Poisson equation, and proceeds to determine the Bohm corrections. The Poisson equation is a gradient equation, and may be treated by the theory of upper and lower solutions developed in [6] and summarized in Appendix A. Notice that the more standard results presented in [28] do not suffice in our situation, since the multipliers of the exponentials in the first equation of (16) are not bounded away from zero. The system for the Bohm corrections is not a gradient system; although it may be analyzed by the conventional tool of geometric invariant regions, we are not aware of any published reference, and we develop this general step more fully. In addition, a proof is provided in Appendix B.2. We now discuss these situations in turn.

Lemma 5.1. *Let $\sigma_{n,\delta}$ and $\sigma_{p,\delta}$ be given functions satisfying (23). Then, problem (16) has a uniquely defined solution φ_δ within the order interval $[\varphi_{min}, \varphi_{max}]$, where the quantities $\varphi_{min} \equiv \inf_\Omega(\underline{\varphi})$ and $\varphi_{max} \equiv \sup_\Omega(\bar{\varphi})$ are independent of δ and the functions $\underline{\varphi}$ and $\bar{\varphi}$ are the solutions of the gradient equations*

$$-\lambda^2 \Delta\underline{\varphi} + \beta_n \exp(\underline{\varphi}) = D_{min} \tag{24}$$

and

$$-\lambda^2 \Delta\bar{\varphi} - \beta_p \exp(-\bar{\varphi}) = D_{max}, \tag{25}$$

to which the boundary conditions (16)$_{2\text{-}3}$ must be adjoined.

Proof. The signs of D_{min} and D_{max} determine the lower and upper bounds for φ_δ. If either $D_{min} > 0$, or $D_{max} < 0$, it is straightforward to define the corresponding bound. However, in the general case, we must apply Lemma A.1 to obtain bounds for the nonlinear Poisson equation. Formally, it is straightforward to see that these functions satisfy the defining conditions for lower and upper solutions. The rigorous derivation of the well-posedness for $\underline{\varphi}$ and $\bar{\varphi}$, together with invariant interval bounds, is obtained as follows. Standard convex analysis, as outlined in the proof of Lemma 3.1 of [18], yields existence and uniqueness for $\underline{\varphi}$ and $\bar{\varphi}$. To prove that these latter functions are in L^∞, we remark that it is enough to show that the exponential functions $\exp(\underline{\varphi})$ and $\exp(-\bar{\varphi})$ are bounded; in this case, Moser iteration theory [14], utilizing L^∞ right-hand sides, implies that the solutions of the redefined *linear* boundary problems are also in L^∞. To illustrate why the exponential function $\exp(\underline{\varphi})$ is bounded, it suffices to assume $D_{min} \leqslant 0$. It can be shown (we omit the details for brevity) that the convex functional with effective L^2 domain in the H^1 affine space defined by boundary trace and restricted by $\exp(\omega) \in L^2(\Omega)$,

$$\frac{\lambda^2}{2} \int_\Omega |\nabla\omega|^2 dx + \beta_n \int_\Omega \{\exp(\omega) - 1\} dx - D_{min} \int_\Omega \omega dx,$$

for which $\underline{\varphi}$ is a minimizer, increases if $\underline{\varphi}$ does not coincide with its upper truncation by the supremum of its (bounded) boundary values. This implies that the exponential is bounded from above; it is bounded below by zero. A similar argument applies to $\bar{\varphi}$ when $D_{max} \geqslant 0$. $\quad\square$

Lemma 5.2. *Let $\tilde{\varphi}_n$ and $\tilde{\varphi}_p$ be given functions in K and let φ_δ be the unique solution of (16) as in Lemma 5.1. Then, problems (17) and (18) have uniquely defined solutions w_δ and z_δ within the order intervals $Q_w = [0, w_{max}]$ and $Q_z = [0, z_{max}]$, resp., w_{max} and z_{max} being the following positive quantities independent of δ*

$$w_{max} = \max\{\sup_{\Gamma_+} w, \exp[(M + \varphi_{max})/2]\},$$

$$z_{max} = \max\{\sup_{\Gamma_+} z, \exp[(M - \varphi_{min})/2]\}.$$

Proof. As each of the nonlinear equations in Steps B and D of the inner iteration loop is not a gradient equation, we employ the theory developed in Appendix B which extends to the case of non-gradient systems the approach of invariant regions. It can be seen that the vector fields associated with the boundary value problems (17) and (18) are Carathéodory mappings and are outward pointing on the respective intervals Q_w, Q_z. Then, applying Theorem B.1 allows one to conclude that each of the maps defined above has a solution with range in the respective Q-interval. A continuous selection principle insures that the mapping is well-defined, as discussed in Appendix C. □

Remark 5.1 (*Positivity of w and z*). Suppose one replaces the boundary values on Γ_0 for w and z in (17)₃ and (18)₃ by strictly positive values, bounded below by δ. Then, using the same arguments as in Lemma 5.2, it can be proved that the solutions w and z of the boundary value problems (17) and (18) belong to the contracted order intervals $[w_{min,\delta}, w_{max}], [z_{min,\delta}, z_{max}]$, resp., where the strictly positive left endpoint $w_{min,\delta}$ (depending on δ) is defined as

$$w_{min,\delta} = \min(\delta_*, \delta, \inf w|_{\Gamma_0 \cup \Gamma_+}),$$

δ_* being the strictly positive quantity satisfying

$$\sup(\bar{\varphi}_n) - \inf(\varphi_\delta) + 2\ln\delta_* < 0$$

(with an analogous relation for $z_{min,\delta}$.)

5.3. Existence of a fixed point for the generalized Gummel map

The analysis of Sections 5.2 and 5.1 has defined a consolidated mapping $\mathbf{T}: K \to K$, in terms of:

(i) Components acting *invariantly on the closed convex subsets of L^2, defined pointwise by the $Q - bounds$* (Inner Iteration Loop, Lemma 5.1 and Lemma 5.2).
(ii) Components acting *invariantly on K* (Outer Iteration Loop, Section 5.1, item (*i*)).

Before continuing our analysis, we need the further following assumption (cf. [17]).

Assumption 5.1 (*Continuous selection hypothesis*). Let (Φ, N, P) denote the components of the mapping $\mathbf{U}$ introduced in Section 3.4. The homotopy mappings for N, P, starting with Laplace's equation, and terminating in a specified solution, are continuous in the L^2 sense with respect to the functions $\tilde{\varphi}_n, \tilde{\varphi}_p, \varphi_\delta$.

A justification of this assumption is provided in Appendix C.
We are then able to state our main theoretical result.

Theorem 5.1. *Under the hypotheses expressed in the bounds of inequalities (23) and the Continuous Selection hypothesis 5.1, the fixed point map defined in (19) has a fixed point in K. Moreover, a solution triple φ, n and p to the BVP (1)–(3) exists in $H^1(\Omega) \cap L^\infty(\Omega)$.*

Proof. By design, the mapping $\mathbf{T}$ of Eq. (20) maps the closed convex set K in $L^2 \times L^2$, introduced in Eq. (7), into itself. The hypotheses of the Schauder fixed point theorem include the continuity and relative compactness of $\mathbf{T}$ in the topology of $L^2 \times L^2$. The relative compactness follows from the action of $\mathbf{R}$ and $\mathbf{W}$ as mappings with bounded range in $H^1(\Omega)$. We shall return to this point at the end of the proof. The continuity of the individual mappings is now considered. The continuity of N, P is part of the content of the Continuous Selection hypothesis. The continuity of Φ is verified as follows. Given two arbitrary pair of elements $[\sigma_n, \sigma_p]$ and $[\sigma_n^*, \sigma_p^*]$ each satisfying (23) where we have suppressed δ-dependence for clarity, consider the images φ and φ^*, resp. Since $\varphi - \varphi^*$ is a test function for the weak formulation, one has

$$\lambda^2 \int_\Omega |\nabla(\varphi - \varphi^*)|^2 dx + \int_\Omega \sigma_n(e^\varphi - e^{\varphi^*})(\varphi - \varphi^*)dx - \int_\Omega \sigma_p(e^{-\varphi} - e^{-\varphi^*})(\varphi - \varphi^*)dx$$

$$= \int_\Omega (\sigma_n^* - \sigma_n)e^{\varphi^*}(\varphi - \varphi^*)dx - \int_\Omega (\sigma_p^* - \sigma_p)e^{-\varphi^*}(\varphi - \varphi^*)dx.$$

The second and third terms on the left hand side are nonnegative. Since the term $\varphi - \varphi^*$ has zero Dirichlet boundary trace, the first term on the left hand side dominates $c\|\varphi - \varphi^*\|_{L^2}^2$, for some constant c. Now, if we utilize the pointwise bounds satisfied by φ^* as stated in Lemma 5.1, and estimate the right-hand side terms by

$$\left| \int_\Omega (\sigma_n^* - \sigma_n) e^{\varphi^*} (\varphi - \varphi^*) dx \right| \leqslant (c/4) \|\varphi - \varphi^*\|_{L^2}^2 + c' \|\sigma_n^* - \sigma_n\|_{L^2}^2,$$

with a similar estimate for the second term, we obtain the L^2 Lipschitz continuity of Φ. The continuity of the mappings $\mathbf{V}_n, \mathbf{V}_p$ follows from their definition in terms of continuous composition. We now consider the continuity of the mappings: $V_n \mapsto \rho, V_p \mapsto \omega$, where V_n, V_p are functions in L^2 restricted by the pointwise bounds for inequalities (23) and those for the range of the mappings N, P. To demonstrate continuity, we consider the first of the two equations. If V_n, V_n^* are given, satisfying the bounds just described, consider the solutions ρ, ρ^*. Since $\rho - \rho^*$ is a test function, the weak formulation leads to

$$\int_\Omega \mu_n e^{V_n} |\nabla(\rho - \rho^*)|^2 dx = \int_\Omega \mu_n (e^{V_n^*} - e^{V_n}) \nabla \rho^* \cdot p \nabla(\rho - \rho^*) dx.$$

To verify L^2 continuity, we employ standard inequalities to obtain, for some constant C, not depending on V_n, V_n^*, ρ, ρ^*,

$$\int_\Omega \mu_n e^{V_n} |\nabla(\rho - \rho^*)|^2 dx \leqslant C \int_\Omega \mu_n |e^{V_n^*} - e^{V_n}|^2 |\nabla \rho^*|^2 dx. \tag{26}$$

We shall now verify sequential continuity. Hold V_n^* and ρ^* fixed and identify V_n and ρ with members of a sequence: $V_n^k \to V_n$. To obtain the gradient convergence of the corresponding ρ^k sequence, we use the fact that a sequence converges to ρ if any subsequence has a further subsequence converging to ρ. Thus, in the right-hand side of (26), we may employ the Lebesgue Dominated Convergence theorem to an appropriate pointwise convergent subsequence of $\{V_n^k\}$ to obtain the convergence to zero of the right-hand side; the corresponding convergence to zero of the left hand side yields the stated sub-sequential convergence. Note that we have used the pointwise bounds derived by the invariant region analysis in a fundamental way to apply the Lebesgue theorem. The analysis for the second mapping parallels this.

We now discuss concisely the H^1 bounds for ρ and ω. Since we assume that the boundary data for ρ is defined in terms of the (bounded) trace of an H^1 function $\overline{\rho}$, we simply use $\rho - \overline{\rho}$ as a test function. This yields:

$$\int_\Omega \mu_n e^{V_n} |\nabla \rho|^2 dx \leqslant \left| \int_\Omega \mu_n e^{V_n} \nabla \rho \cdot \nabla \overline{\rho} dx \right|.$$

Standard inequalities give a fixed gradient bound in terms of $\overline{\rho}$. Since the trace is specified, one has the desired H^1 bound, hence the relative compactness. The arguments for ω are similar. Schauder's fixed point theorem [14, Corollary 10.2, p. 222] gives the existence of a fixed point. □

5.4. Theoretical remarks on the GGM

It seems clear that a viable approach to the analysis of the GGM proposed in this work is represented by the 'a priori' bounds (23) for $\sigma_{n,\delta}, \sigma_{p,\delta}$. These estimates permit a well-defined fixed point for the inner iteration map, and can be physically justified by noting that $\sigma_n = \rho \exp(G_n)$. As the quantum correction G_n is expected to be negligible far from the material interface Γ_0 and to rapidly diverge towards $-\infty$ at Γ_0, it is immediate to see that $\sigma_n \geqslant 0$ in $\overline{\Omega}$, the equality holding *only* at Γ_0, while elsewhere in the device domain σ_n tends to coincide with the Slotboom variable in the classical DD case.

One further issue concerning the solution of the Bohm Eqs. (17) and (18) not yet emphasized in the preceding discussion is the positivity of the solution in the interior of the domain Ω, which in our analysis is the result of Lemma 5.2 and of the related Remark 5.1. For an alternative approach, we refer the reader to [22], where a continuous minimum principle is proved to hold for the solutions of the Bohm Eqs. (17) and (18), provided that the semi-linear terms satisfy a suitable lower bound (cf. [22], Assumption B.3).

6. The discretized model and the numerical GGM

In this section, we describe the finite element discretization of the differential subproblems involved in the GGM introduced in Sections 3.2, 3.3 and 3.4. With this aim, we denote by $\mathcal{T}_h$ a given regular partition of the domain Ω (cf. [7]) into non-overlapping triangles K of diameter h_K, and we indicate by $h = \max_{K \in \mathcal{T}_h} h_K$ the discretization parameter. Then, we introduce the finite dimensional subspace $\mathcal{V}_h \subset \mathcal{V}$ of affine finite elements over $\mathcal{T}_h$, and for a given function $\phi : \mathcal{T}_h \to \mathbb{R}$, we let $\Pi_h \phi \in \mathcal{V}_h$ be the interpolant of ϕ mapping into $\mathcal{V}_h$.

6.1. The finite element maps

Each of the boundary value problems involved in the steps of the Inner and Outer iteration loops is approximated with the Galerkin finite element method (GFEM) using basis functions in $\mathcal{V}_h$.

Let us start with Step (1) of the Outer Iteration Loop of Section 3.2. This requires executing the Inner Iteration Loop of Section 3.4.

Step (A) requires the solution of the nonlinear Poisson equation (16). This is done through the Newton method with the introduction of a proper damping technique to ensure that the iteration is a descent method (cf. [35], Chapter 7). The resulting algebraic system is characterized by having a symmetric positive definite and diagonally dominant coefficient matrix,

provided that a lumping procedure is employed to treat the zeroth order term arising from the linearization of (16). Steps (B) and (C) are a critical issue of the algorithm, because of the need of maintaining positive solutions for the (square root) of the carrier densities. With this aim, we have modified the standard Newton procedure by introducing a relaxation parameter, to be chosen in such a way that the finite element approximation of the linearized boundary value problem enjoys a discrete maximum principle (DMP). This is a sufficient condition to ensure positivity of the computed approximate carrier concentrations. Details of the procedure can be found in [11,10]. The finite element approximation of Steps (A), (B) and (C) defines the numerical map $\mathbf{U}_h : (\mathcal{V}_h)^2 \to (\mathcal{V}_h)^3$.

Once Step (1) is implemented as described above, the numerical approximation of the remaining linear continuity equations (Step (3) of the Outer Iteration Loop of Section 3.2) is carried out by the GFEM with harmonic average along the element edges of the diffusion coefficient $\mu_v \exp(\pm V_{v\delta,h})$, $v = n, p$ [19,11,10]. The actual implementation is carried out with the addition of the change of discrete variables

$$n_h = \rho_h \exp(V_{n\delta,h}), \quad p_h = \omega_h \exp(-V_{p\delta,h})$$

in order to prevent the occurrence of numerical overflows. This approach is a consistent multi-dimensional generalization of the classical one-dimensional Scharfetter–Gummel difference scheme [34]. It has the advantage of automatically introducing an upwinding treatment of the carrier densities along triangle edges, which in turn ensures that the method satisfies a DMP with positive nodal values of the carrier densities n and p, under the assumption that μ_n and μ_p are constant and that $\mathcal{T}_h$ is of Delaunay type (see [33,5,13] for a thorough discussion of this latter subject). The finite element approximation of Step (3) defines the numerical maps $\mathbf{R}_h : \mathcal{V}_h \to \mathcal{V}_h$ and $\mathbf{W}_h : \mathcal{V}_h \to \mathcal{V}_h$.

6.2. The numerical fixed point map

The numerical GGM can be written in abstract form as

$$\mathbf{T}_n := [-\ln_h \mathbf{R}_h \circ \mathbf{V}_{n,h} \circ \mathbf{U}_h, \ln_h \mathbf{W}_h \circ \mathbf{V}_{p,h} \circ \mathbf{U}_h], \tag{27}$$

where $\ln_h(\cdot) := \Pi_h(\ln(\cdot))$ and $\mathbf{V}_{n,h}$, $\mathbf{V}_{p,h}$ are the discrete counterparts of the maps $\mathbf{V}_n$, $\mathbf{V}_p$ introduced in Section 3.4.

6.3. Convergence for the numerical fixed point map

We discuss the general question of whether the fixed points $\mathbf{x}_n$ of $\mathbf{T}_n$ converge to the desired fixed point $\mathbf{x}_0$ of $\mathbf{T}$. Here, we refer to the mappings defined in (27) and in (20), resp. In the linear theory, the Babuška–Brezzi inf–sup theory permits one to transfer the corresponding question to one of best approximation, i.e., consistency of the approximating Galerkin subspace. The Krasnosel'skii theory [24,25] is the analog for nonlinear differentiable problems: one may assert that $\mathbf{x}_n \to \mathbf{x}_0$ at the rate at which $\mathbf{T}_n$ approximates $\mathbf{T}$ (discretization order), provided a set of stability conditions associated with the operator differential calculus are satisfied. It is known that the theory of Babuška–Brezzi is strictly implied by the theory of Krasnosel'skii. In the present case, the maximal order of convergence with respect to the discretization parameter h in the energy norm is $O(h^v)$, with $v \in (0, 1]$ (cf. [19], Section 5.3.2), that is exactly the expected order for the linear mixed boundary value problem. An extensive analysis is required to establish the hypotheses, summarized in [19, p. 119]. Although $\mathbf{T}_n$ differs from the mapping of the classical model in its inclusion of the quantum correction terms, we expect a carry-over of the convergence rate, for fixed $\delta > 0$. The verification is outside the scope of the current study.

7. Numerical assessment of the GGM

In this section, we present a set of numerical examples to validate the GGM procedure in the simulation of realistic nanoscale devices. In Section 7.1, we analyze the convergence properties of the inner loop of the GGM procedure applied to a one-dimensional (1D) test case, with the purpose of demonstrating the plausibility of assumptions (23). In Section 7.2, we study the convergence properties of the full GGM algorithm applied to the simulation of a two-dimensional (2D) device with the same geometry as in Fig. 1, with special care on the dependence of such properties on the truncation parameter δ. Finally, in Section 7.3 we illustrate the relevance of QCDD models for the simulation of advanced CMOS structures. With this purpose, a nanoscale device with intrinsically 3D geometry is presented together with a short discussion of its electrical characteristics as predicted by computations performed using the DD, QDD and Schrödinger–Poisson DD (SPDD) models.

7.1. A nanoscale one-dimensional MOS capacitor

In this section we consider a 1D test case that can be regarded as a cross–section of the device of Fig. 1 in the direction connecting the bulk contact (bottom portion of Γ_+) to the interface contact Γ_0. As no current is expected to flow across the interface, the quasi-Fermi levels are known a priori to be constant, so that we only need to solve the Poisson–Bohm subsystem (8) and only the Inner Iteration Loop of the GGM needs to be executed. The device length is of 100 nm, the doping is of p-type and has a concentration of 10^{21} m^{-3}, and the boundary conditions for the potential are $\varphi_{\text{bulk}} = 0$ V, $\varphi_{\text{interface}} = 0.1$ V. A nonuniform mesh with a step-size varying gradually from a maximum of 7.9168×10^{-9} m at the bulk contact to a

minimum of 1.7347 × 10⁻¹⁴ m at the interface side of the device was used for the computations. Fig. 3 (left) shows that the dependence of the computed electron density on the truncation parameter δ is almost negligible, and that the variation of the quantum correction G_n significantly occurs only across the mesh element closest to the interface (Fig. 3, right). Fig. 4 (left) shows that the *a priori* bound (23) for σ_n is actually consistent with the physics, as $\sigma_n = 1$ in the whole device except in the region corresponding to the steep boundary layer at the interface where it rapidly decreases to $\sigma_n = 0$. Finally, Fig. 4 (right) shows that decreasing the value of δ only slightly affects the convergence rate of the iteration scheme. Nevertheless, given the almost linear rate of convergence, the use of vector extrapolation techniques is expected to produce a noticeable reduction in the number of required iterations (see Ref. [10]).

7.2. Experimental convergence analysis on a two-dimensional device

In this section, we perform an experimental convergence analysis of the Outer Iteration Loop of the GGM. Reported computations refer to the 2D simulation of a device with the same structure as that of Fig. 1, having length in the *x* and *y* directions equal to 75 nm and 100 nm, respectively. The piecewise constant doping profile of the device is shown in Fig. 5. The *n*-type dopant in the source and drain regions has a concentration of 10^{25} m⁻³ while in the rest of the domain the doping is of *p*-type and has a concentration of 10^{21} m⁻³. Also shown in Fig. 5 is the nonuniform computational mesh which has a step-size gradually decreasing near the upper side of the domain boundary. The computational results in Figs. 6 and 7 refer to the device biased in the off-state condition. The applied voltages in this case are 0.1 V at the drain and gate contact and 0 V at the source and bulk contacts. In this regime, there is no conductive path between the source and drain contacts, which can be clearly seen from Fig. 6(c) where the potential barrier under the gate contact is visible and in Fig. 6(b) which shows that there is no inversion layer at the gate. It is to be noted that, consistently with the discussion carried out in the theoretical part of the present paper, the Poisson and Bohm equations have been solved with a Dirichlet boundary condition applied at the gate contact (see Fig. 6(b) and (c)) while the current continuity equation has been solved with an homogeneous Neumann boundary condition at the gate contact, as is apparent from the spatial distribution of the electron quasi-Fermi level shown in Fig. 6(a). Fig. 7 shows the spatial distribution of the electron Bohm potential G_n in the device in the off-state condition, corresponding to two different values of the truncation parameter δ. The results show that G_n is vanishing everywhere in the domain except in the steep boundary layer near the gate contact, where it attains an absolute value of about 1.5 V, and that the value of G_n at the contact depends on the truncation parameter, becoming larger, as expected, as $\delta \to 0$. Fig. 8 shows the quantity e_k defined as

$$e_k := \max(\|\delta\varphi^{(k)}\|_{L^\infty(\Omega)}, \|\delta\varphi_n^{(k)}\|_{L^\infty(\Omega)}, \|\delta\varphi_p^{(k)}\|_{L^\infty(\Omega)}, \|\delta G_n^{(k)}\|_{L^\infty(\Omega)}, \|\delta G_p^{(k)}\|_{L^\infty(\Omega)}) \tag{28}$$
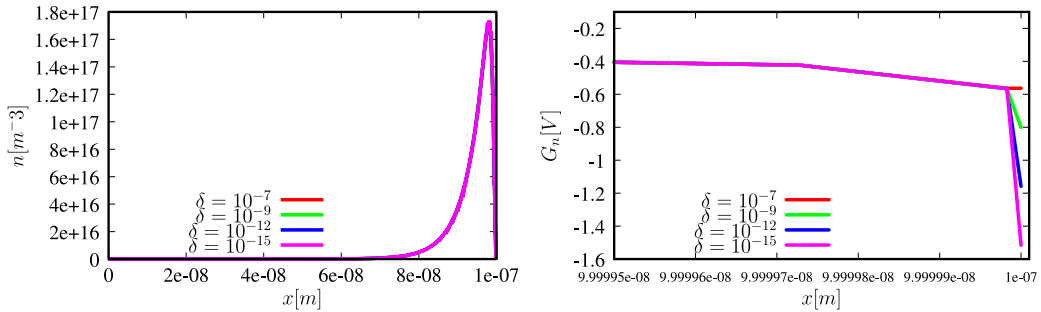

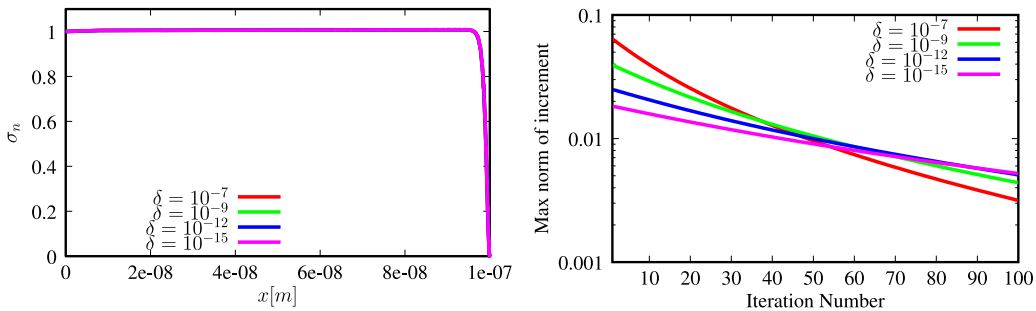**Fig. 3.** Left: electron concentration in the device; right: Bohm potential near Γ_0.

Fig. 4. Left: spatial distribution of σ_n; right: convergence rate of the inner loop of the GGM as a function of the truncation parameter δ.
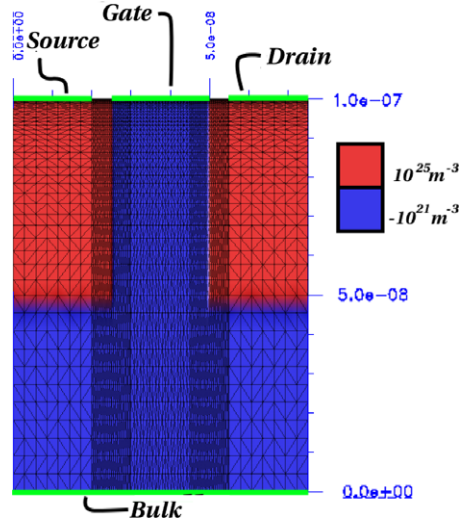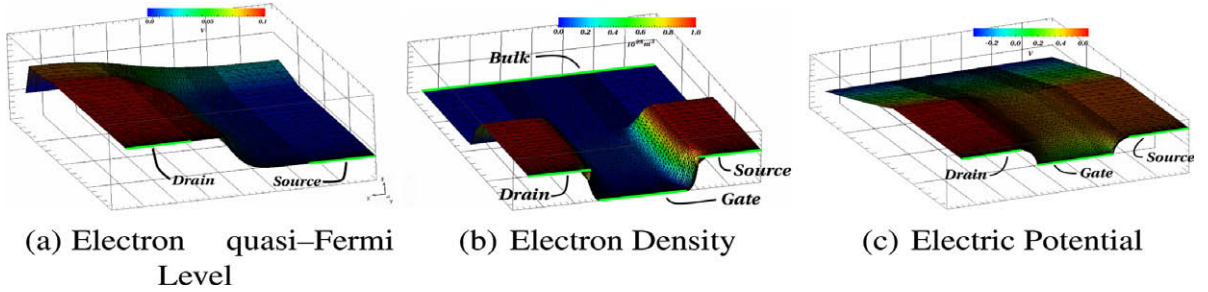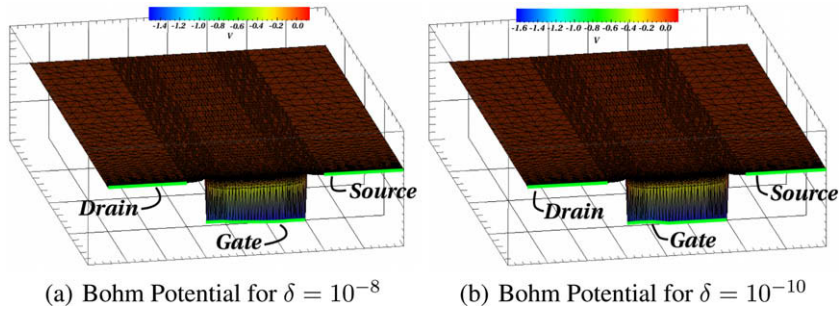
Fig. 5. Doping profile and computational grid.

(a) Electron   quasi–Fermi   Level

(b) Electron Density

(c) Electric Potential

Fig. 6. Simulation results for $V_{drain} = V_{gate} = 0.1$ V.

(a) Bohm Potential for $\delta = 10^{-8}$

(b) Bohm Potential for $\delta = 10^{-10}$

Fig. 7. Results for $V_{drain} = V_{gate} = 0.1$ V.

as a function of the iteration number k. In (28), $\delta(\cdot)^{(k)}$ denotes the increment of each quantity from iteration k to $k + 1$. From Fig. 8 one can see that the convergence rate of the outer loop is almost linear and that it changes slightly when the truncation parameter is modified.

Figs. 9 and 10 show results of a simulation performed with the device biased in the on-state condition. By comparing Fig. 6(c) with Fig. 9(b) one may notice that the potential barrier between source and drain has disappeared. This causes electrons to accumulate near the gate contact, forming the inversion layer which is visible in Fig. 9(a). Fig. 9(c) displays a close-up view of the channel of the device with the direction (arrows) and magnitude (color) of the electron current density and shows that the shift of the charge peak due to the boundary condition imposed on Γ_0 causes the current to flow away from the boundary. The graphs in Fig. 10 show that the Bohm potential in the on–state regime becomes very large in absolute
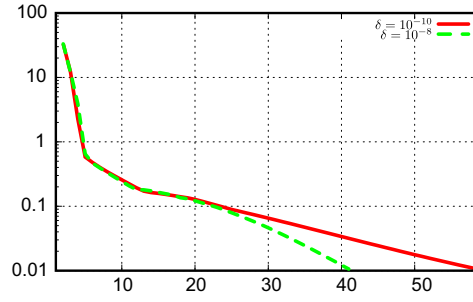
Fig. 8. Convergence history for $V_{drain} = V_{gate} = 0.1$ V.

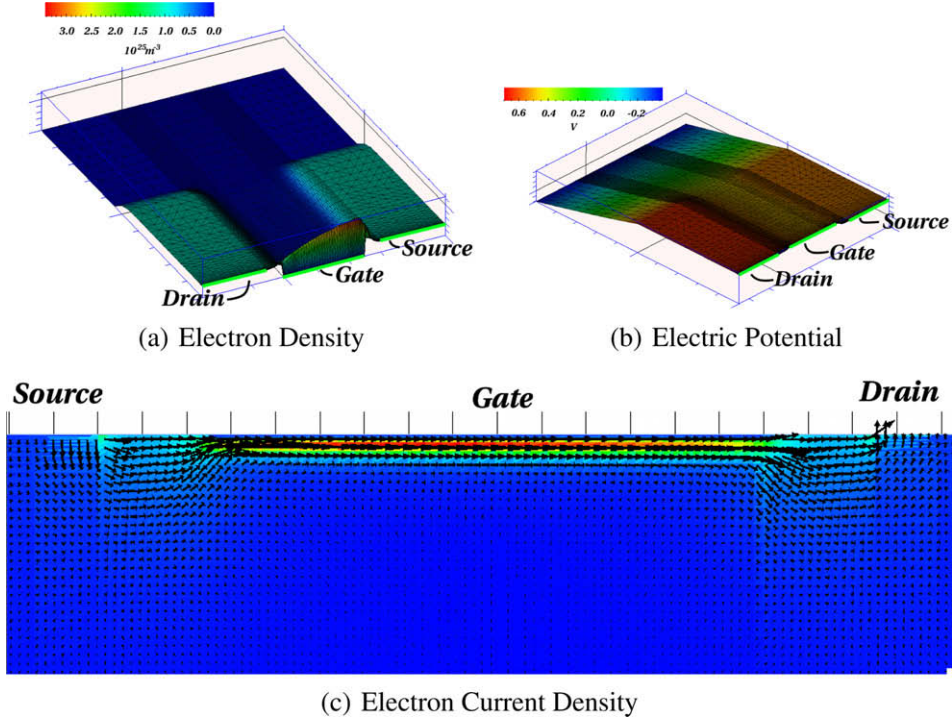(a) Electron Density

(b) Electric Potential

(c) Electron Current Density

Fig. 9. Simulation results for $V_{drain} = 0.1$ V, $V_{gate} = 0.7$ V.

(a) Bohm Potential for $\delta = 10^{-8}$

(b) Bohm Potential for $\delta = 10^{-10}$

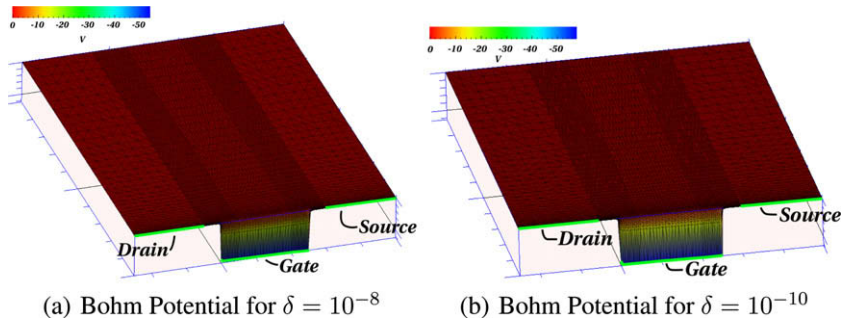**Fig. 10.** Results for $V_{drain} = 0.1$ V, $V_{gate} = 0.7$ V.

value (more than 50 V) and negative at the gate contact, but still vanishes elsewhere in the device domain as was the case in the off-state regime. It is also to be noticed that, compared to the very large value attained by G_n at this bias, its variation due to the choice of the truncation parameter is almost negligible. Finally, Fig. 11 shows that the convergence rate of the outer loop is almost linear also in the on-state condition, and that it changes slightly when the truncation parameter is modified.
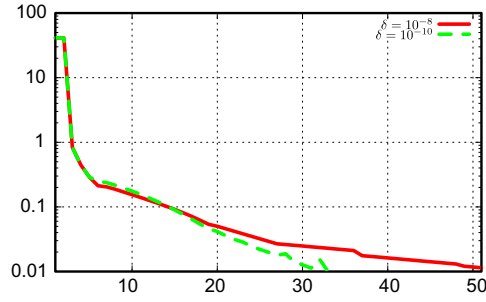
Fig. 11. Convergence history $V_{\text{drain}} = 0.1$ V,$V_{\text{gate}} = 0.7$ V.

7.3. QCDD simulation of a three-dimensional device

The purpose of this section is to demonstrate the relevance of including the quantum correction terms G_n and G_p in the simulation of a realistic nanoscale device in terms of their impact on the electrical performance of the device. Also, to assess the performance of the QDD model both in terms of accuracy and computational cost, we compare the simulation results obtained by the QDD model with those of both a simpler (thus less computationally expensive) model, namely the DD model, and those of a more accurate (but more computationally complex) model, namely the SPDD model [11].

The chosen device is a 3D double-gate MOSFET [36] with the following geometry:

- Silicon film thickness $T_{Si} = 10$ nm.
- Gate length $L_g = 13$ nm, channel length $L_{CH} = 11$ nm.
- Oxide thickness $T_{OX} = 2$ nm.
- Total Source-to-Drain length $L = 49$ nm.
- Width $W = 20$ nm.

The doping profile D is a piecewise constant function and has a value equal to $N_D^+ = 5 \times 10^{25}$ m^{-3} in the source and drain regions and equal to $-N_A^- = -10^{21}$ m^{-3} in the channel region, respectively. These values are consistent with the indications of the latest release of the ITRS [8].

Fig. 12 displays the device geometry and the finite element mesh used in the numerical computations, while the log scale values of the doping profile are tabulated on the right-hand side color-bar. The computational grid consists of 89136 tetrahedra (18081 mesh nodes). Fig. 13 shows the I–V (current–voltage) curves obtained from full 3D simulations with the DD, QDD and SPDD models, respectively, with the purpose to highlight the non-negligible difference between a classical and a quantum-corrected simulation for the given device geometry which, in turn, clearly indicates the importance of taking into account electrostatic quantum effects in such aggressively scaled devices. In Fig. 13(a) on the x-axis the value of the applied Gate voltage V_g is tabulated, while on the y-axis the value of the computed Drain current is plotted in logarithmic scale for a value of the voltage applied at the Drain of $V_d = 10$ mV. From this picture one can notice that the curve corresponding to the QDD model results has degraded slope in the sub-threshold region in comparison to the prediction of the DD model. Fig. 13(b) shows the results of the same computations as above but with the y-axis in linear scale; from this picture one can see that the QDD model predicts a larger value of the threshold voltage compared to the classical simulation, which is an expected consequence of the increased effective oxide thickness. Although both effects are underestimated by the QDD model in comparison to a more accurate SPDD simulation, one might argue that the largely inferior computational effort required by the QDD model compared to the SPDD model for a full 3D simulation more than compensates the slight inaccuracy in the current prediction. In fact, the computation of each bias point required about 10 min with the DD model,
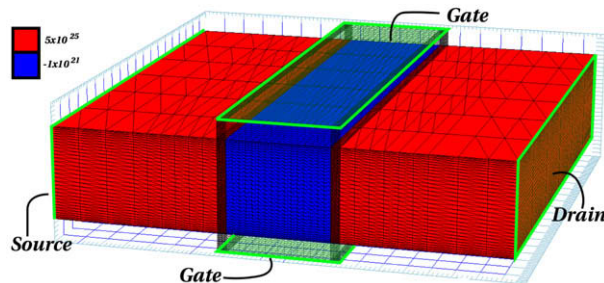

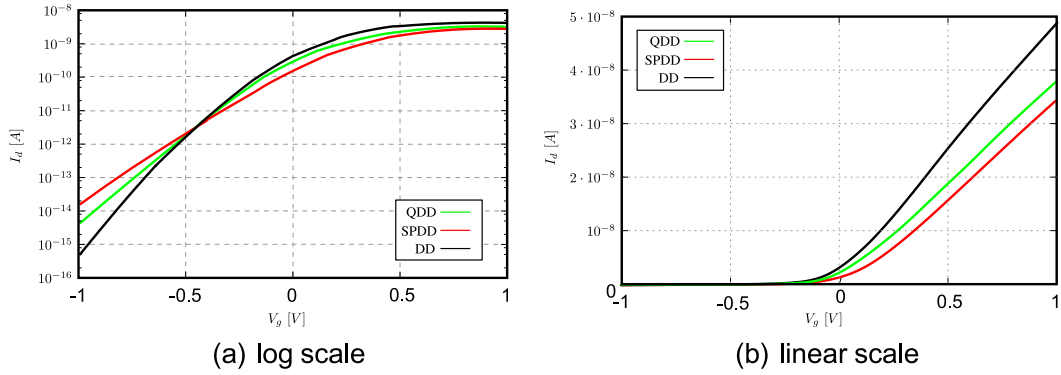**Fig. 12.** Device geometry, doping profile and computational mesh.

Fig. 13. Drain current I_d vs. Gate voltage V_g for the biasing conditions $V_d = 0.01$ V and $V_s = 0$ V.

(a) Section parallel to the x-z plane   (b) Section parallel to the y-z plane
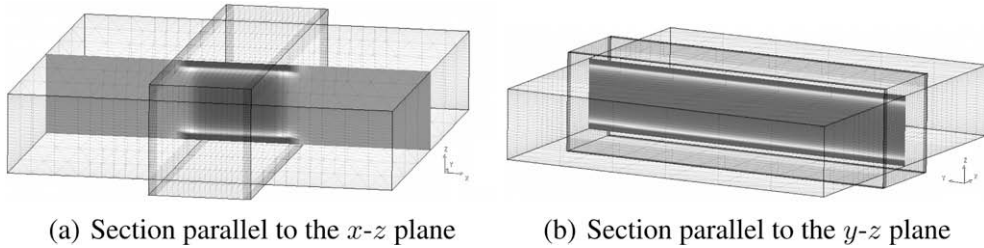
Fig. 14. Electron density in the device computed by the QDD model at the biasing conditions $V_d = 0.01$ V and $V_g = V_s = 0$ V; lighter shades of gray indicate higher values of the density.

up to 45 min with the QDD model and more than 3 h with the SPDD model.[4] Finally, Fig. 14 shows the electron density in the device computed by the QDD model at the biasing conditions $V_d = 0.01$ V and $V_g = V_s = 0$ V, the charge peak-shift effect being evident in both pictures.

8. Conclusions and future perspectives

In this article, we have addressed the analysis of existence of a fixed point of the functional iteration procedure (GGM) for the solution of QCDD models, proposed and thoroughly numerically investigated in [11]. Several numerical examples have also been included to support the theoretical conclusions. The GGM has the benefit of maintaining the same functional structure irrespective of the specific choice of the quantum-corrected model, and, in the case of the QDD model, to provide an effective computational tool for the numerical solution of the variational formulation proposed in Refs. [1,31] to treat the quantum correction. The principal instruments used in the analysis are (i) the introduction of a truncation operator; (ii) the extension of the theory of invariant regions, used in [19] in the DD case; and (iii) a homotopy method based on the general theory developed in [17] to select the solution of each equation yielding the quantum corrections. It is expected that, with some modifications, the framework proposed in the present work can be extended to deal with other quantum-corrected models, as considered in [11,23,29,30]. This extension will be the object of a future study.

Appendix A. Upper and lower solutions for gradient equations

We cite in this section the essential results developed in [6]. Let $\Omega \subset \mathbb{R}^N$ be a bounded domain with piecewise-C^1-boundary $\partial\Omega$, and $\Gamma_N \subset \partial\Omega$ be such that $\Gamma_D = \partial\Omega \setminus \Gamma_N$ is a relatively open C^1-portion of $\partial\Omega$ with positive surface measure. Consider the boundary value problem (BVP)

$$-\operatorname{div}(a(x)\nabla u) + f(x, u) = 0 \text{ in } \Omega, \tag{A.1}$$

$$u = u_D \text{ on } \Gamma_D, \quad \frac{\partial u}{\partial \nu} + g(x, u) = 0 \text{ on } \Gamma_N, \tag{A.2}$$

where $a \in L^\infty(\Omega)$ with $a(x) \geqslant \mu > 0$, and $\partial/\partial\nu$ denotes the outward conormal derivative on Γ_N. Let $H := W^{1,2}(\Omega)$ denote the usual (real) Sobolev space, and let $H_0 \subset H$ be the subspace of H defined by

---

[4] The code used for the simulation is a set of Octave scripts and was run on a MacBook laptop with a 2 GHz CPU and 1 Gb RAM with Octave 2.9.17.

$$H_0 = \{u \in H | \gamma u = 0 \text{ on } \Gamma_D\},$$

where $\gamma : H \to L^2(\partial\Omega)$ is the trace operator which is linear and compact. The corresponding dual spaces are denoted by H^* and H_0^*. It is known that $\|u\|_{H_0}^2 = \int_\Omega |\nabla u|^2 dx$ defines an equivalent norm on the subspace H_0. We assume the boundary values u_D to be the restriction of a function $\tilde{u}_D \in H$, i.e., $\tilde{u}_D|_{\Gamma_D} = u_D$.

(C1) We assume the nonlinearities f and g in (A.1) and (A.2), respectively, to be of Carathéodory type. We assume f and g are increasing in u.

The weak formulation of the BVP (A.1) and (A.2) reads as follows.

Definition A.1. $u \in H$ is called a *solution* of the BVP (A.1) and (A.2) if

(i) $u = u_D$ on Γ_D, and
(ii) $\int_\Omega a\nabla u \cdot \nabla\psi dx + \int_{\Gamma_N} g(x, \gamma u)\gamma\psi d\Gamma + \int_\Omega f(x, u)\psi dx = 0, \ \forall \ \psi \in H_0$.

Let us recall for convenience the notion of (weak) super- and sub-solutions.

Definition A.2. $\bar{u} \in H$ is called a *supersolution* of the BVP (A.1) and (A.2) if

(i) $\bar{u} \geqslant u_D$ on Γ_D, and
(ii) $\int_\Omega a\nabla\bar{u} \cdot \nabla\psi dx + \int_{\Gamma_N} g(x, \gamma\bar{u})\gamma\psi d\Gamma + \int_\Omega f(x, \bar{u})\psi dx \geqslant 0, \ \forall \ \psi \in H_0 \cap L_+^2(\Omega)$,

Similarly, $\underline{u} \in H$ is a *subsolution* if the reversed inequalities in Definition A.2 hold with $\bar{u}$ replaced by $\underline{u}$. We make the following additional hypotheses.

(C2) There exist a supersolution $\bar{u}$ and a subsolution $\underline{u}$ of the BVP (A.1) and (A.2) such that $\underline{u} \leqslant \bar{u}$.
(C3) There is a $p \in L_+^2(\Omega)$ such that $|f(x,s)| \leqslant p(x)$ for a.e. $x \in \Omega$ and $s \in [\underline{u}(x), \bar{u}(x)]$.
(C4) There is a $q \in L_+^2(\Gamma)$ such that $|g(x,s)| \leqslant q(x)$ for a.e. $x \in \Gamma$ and $s \in [\gamma\underline{u}(x), \gamma\bar{u}(x)]$.

The following lemma was established in [6].

Lemma A.1. *Under the hypotheses (C1)–(C4), the BVP (A.1) and (A.2) has a uniquely defined solution u within the order interval $[\underline{u}, \bar{u}]$.*

Appendix B. Invariant regions for non-gradient systems

We consider in this section the following nonlinear system of *m steady-state nonlinear reaction-diffusion equations* on a bounded Lipschitz domain $\Omega \subset \mathbf{R}^N$

$$\Delta\mathbf{u} = \mathbf{f}(\cdot p, \mathbf{u}), \mathbf{u} = (u_1, \ldots, u_m)^T, \mathbf{f} = (f_1, \ldots, f_m)^T, \tag{B.1}$$

where Δ denotes the Laplacian, acting on each component. System (B.1) is supplied with mixed boundary conditions as follows.

(i) *Dirichlet Boundary*. There is a (relatively open) boundary component Γ_D such that the restriction of $\mathbf{u}$ to Γ_D agrees with a smooth function $\hat{\mathbf{u}} \in C^\infty(\overline{\Omega})$, with range in Q:

$$\gamma(\mathbf{u} - \hat{\mathbf{u}})|_{\Gamma_D} = 0. \tag{B.2}$$

Here, γ denotes the trace operator.
(ii) *Neumann Boundary*. The normal derivative of $\mathbf{u}$ vanishes in a weak sense on the complement of Γ_D with respect to $\partial\Omega$. This is a natural boundary condition subsumed in the weak formulation.

Our aim is *to extend to* (B.1) the theory of super-and sub-solutions for linear elliptic equations.

B.1. Generalities

For this, we characterize the structure of the vector field $\mathbf{f}$.

(1) *Carathéodory Mapping (CM)* Define the slab,

$$Q = \prod_1^m [a_i, b_i], \quad a_i < b_i, \quad i = 1, \ldots, m,$$

in $\mathbf{R}^m$ and the Cartesian product, $D_0 = \Omega \times Q$. $\mathbf{f}$ is assumed to be a Carathéodory mapping (CM) on D_0.

(2) *Outward Pointing on the Boundary of Q (Property OP)*.

If $u_i = a_i, \quad i = 1, \ldots, m, \quad$ then $f_i(\cdot, u_1, \ldots, u_m) \leqslant 0$;

if $u_i = b_i, \quad i = 1, \ldots, m, \quad$ then $f_i(\cdot, u_1, \ldots, u_m) \geqslant 0$.

The following result will be proved in the following section.

Theorem B.1 (Existence, with range in invariant regions). *Suppose* $\mathbf{f}$ *satisfies properties* CM *and* OP, *and is* L^2 *bounded as a composition mapping. Then* (B.1) *and* (B.2) *has a weak solution* $\mathbf{u}$ *with range in Q.*

B.2. A trapping principle for semi-linear elliptic systems

We consider again system (B.1). This framework has a significant implication, due to Krasnosel'skii. We state it in the form of a lemma.

Lemma B.1. *For a Carathéodory mapping h, if h maps (a subset of)* $L^2(\Omega)$ *into* $L^2(\Omega)$, *via the composition,* $H(\mathbf{v}) = h(\cdot p, \mathbf{v})$, *then H defines a continuous mapping from* L^2 *to* L^2.

This was shown by Krasnosel'skii [24, Theorem 2.1, p. 22] (see also [12, p. 77]).

Since we may identify the components of $\mathbf{f}(\cdot p, \mathbf{u})$ with elements of L^2, then we may identify these components with continuous linear functionals on H^1. In this identification, it is necessary to use the equivalent norms on $Y_i = H^1$, given by

$$(v, w)_{Y_i} = \int_\Omega \nabla v \cdot p \nabla w dx + \int_{\Gamma_D} \gamma v \gamma w d\sigma. \tag{B.3}$$

In order to define what is meant by weak solution, we introduce the inner product on $Y = \prod_1^m Y_i$ as

$$(\mathbf{v}, \mathbf{w})_Y = \sum_1^m \int_\Omega p_i \nabla v_i \cdot p \nabla w_i dx + \sum_1^m \int_{\Gamma_D} \gamma v_i \gamma w_i d\sigma. \tag{B.4}$$

We identify the zero trace subspace of Y:

$$Y_0 = \{\mathbf{v} \in Y : \gamma \mathbf{v}|_{\Gamma_D} = \mathbf{0}\}.$$

Then $\mathbf{u}$ is a weak solution of (B.1) and (B.2) if $\mathbf{u}$ satisfies (B.2) and the relation,

$$(\mathbf{u}, \phi)_Y + \langle \mathbf{f}(\cdot p, \mathbf{u}), \phi \rangle = 0, \forall \phi \in Y_0. \tag{B.5}$$

Here, the duality relation is used with component summation.

B.2.1. The variational inequality

We begin by establishing some notation. We set

$$\mathbf{K}_0 = \{\mathbf{v} \in Y : \gamma(\mathbf{v} - \hat{\mathbf{u}})|_{\Gamma_D} = \mathbf{0}, \mathbf{v}(x) \in Q \text{ for almost all } x \in \Omega\}. \tag{B.6}$$

The variational inequality can be formulated as: Determine $\mathbf{u} \in \mathbf{K}_0$ such that, if $F(\mathbf{u}) = \mathbf{f}(\cdot, \mathbf{u})$, then

$$\langle F(\mathbf{u}), \mathbf{v} - \mathbf{u} \rangle + (\mathbf{u}, \mathbf{v} - \mathbf{u})_Y \geqslant 0, \quad \forall \mathbf{v} \in \mathbf{K}_0. \tag{B.7}$$

Parallel to Theorem B.1 is the following proposition.

Proposition B.1. *Suppose* $\mathbf{f}$ *satisfies property* (CM), *and is componentwise* L^2 *bounded. Then the variational inequality* (B.7) *has a solution* $\mathbf{u} \in \mathbf{K}_0$.

We shall deduce Proposition B.1 from quadratic minimization, in conjunction with the Schauder fixed point theorem in the following subsections.

B.2.2. Existence for the variational inequality

We define the closed convex sets $\mathbf{K}_i \subset Y_i, i = 1 \ldots, m$, by

$$\mathbf{K}_i = \{v \in Y_i : \gamma(v - \hat{u}_i)|_{\Gamma_D} = 0, v(x) \in [a_i, b_i] \text{ for almost all } x \in \Omega\}. \tag{B.8}$$

We notice that

$$\mathbf{K}_0 = \prod_1^m \mathbf{K}_i.$$

If $K_0 = \{\mathbf{v} \in \prod_1^m L^2 : \mathbf{v}(x) \in Q \text{ for almost all } x \in \Omega\}$, we define a map

$$T : K_0 \mapsto \mathbf{K}_0$$

as follows. Set $T\mathbf{w} = \mathbf{u}$ if $\mathbf{u}$ solves the decoupled variational inequality: Determine $\mathbf{u} \in \mathbf{K}_0$ such that, if $F(\mathbf{w}) = \mathbf{f}(\cdot, \mathbf{w})$, then

$$\langle F(\mathbf{w}), \mathbf{v} - \mathbf{u} \rangle + (\mathbf{u}, \mathbf{v} - \mathbf{u})_Y \geqslant 0, \quad \forall \mathbf{v} \in \mathbf{K}_0. \tag{B.9}$$

In order to analyze this inequality, we first isolate an arbitrary inequality of the decoupled system. Using the notation, for fixed i,

$$u_i = u, \quad v_i = v, \quad w_i = w, \quad F_i(\mathbf{w}) = G, \quad \hat{u}_i = \hat{u},$$

we determine a unique element v_0 via the Riesz representation theorem such that

$$\langle G, \phi \rangle = (v_0, \phi)_{Y_i}. \tag{B.10}$$

By standard results concerning quadratic minimization over closed convex sets, u may be characterized as the unique element minimizing the functional,

$$\Phi(v) = \|v - v_0\|^2 - \|v_0\|^2,$$

over $\mathbf{K}_i$. We easily obtain an 'a priori' estimate for $u \in Y_i$.

We are now ready to verify the existence of a solution of the variational inequality. In order to apply the Schauder fixed point theorem, we require the components of the image of T to lie in closed, compact sets in L^2, and for T to be continuous (see [14, Theorem 10.1]). The intersection of $\mathbf{K}_i$ with the ball in Y_i, described by an 'a priori' estimate, is relatively compact in the closed convex set $K_0 \subset \prod_1^m L^2$ by the compact embedding. Thus, it remains to verify the continuity of T. By appropriately subtracting the inequalities corresponding to two distinct solutions $\mathbf{u}^* = T\mathbf{w}^*, \mathbf{u}^{**} = T\mathbf{w}^{**}$, we finally obtain, for some positive constant C,

$$\|\mathbf{u}^* - \mathbf{u}^{**}\|_Y^2 \leqslant C\|F(\mathbf{w}^*) - F(\mathbf{w}^{**})\|^2$$

By use of Lemma B.1, we infer the continuity of T on $\prod_1^m L^2$. Application of the Schauder theorem concludes the proof.

B.2.3. Major equivalence theorem

In this section, we use the property (OP) satisfied by the vector field $\mathbf{f}$ to assert that a solution of the variational inequality (B.6) is a weak solution of the system (B.1) and (B.2), i.e., satisfies (B.5). For details, cf. [19].

Theorem B.2. *Let $(u_1, \ldots, u_m)^T$ be a solution of (B.7). Then, under the hypothesis (OP) on $\mathbf{f}$, $(u_1, \ldots, u_m)^T$ is a solution of (B.5). In particular, Theorem B.1 holds.*

Appendix C. Continuous selection hypothesis

The justification of Assumption 5.1 is outlined in this section. Without loss of generality, we consider the second equation of (8). If the consolidated Dirichlet boundary is denoted by Γ_D, we denote by w_{bdy} the consolidated Dirichlet boundary data. We write the trivial homotopy for the second equation of (8), inclusive of boundary condition, in the operator format (with subscripts suppressed for simplicity):

$$F(w, \lambda) = [-\delta^2 \Delta w + \lambda f(x, w) = 0, \text{Dirichlet trace} = w_{\text{bdy}}], 0 \leqslant \lambda \leqslant 1.$$

The first component of $[\cdot, \cdot]$ is understood in the weak sense: H^1 is mapped into its dual $[H^1]^*$. We summarize the theory of [17], especially Theorem 3.1. Under a minimal set of hypotheses:

  (i) F_w is locally Lipschitz continuous;
 (ii) there are locally defined linear approximate right inverses G of F_w, which are uniformly bounded in norm;
(iii) the family $\{G\}$ satisfies an approximation of the identity condition;

it is demonstrated in [17] that a discrete homotopy path exists over the interval $[0, 1]$ for F, permitting the precise 'capture' of a zero of $F(\cdot, 1)$. The argument presumes a sufficiently small residual at $\lambda = 0$, and employs a predictor/corrector 'algorithm' with N_0 steps to reach a starting iterate in the domain of convergence of Newton's operator method at $\lambda = 1$. The predictors are denoted $\{v_i\}_1^{N_0}$ and the correctors, including the starting iterate, $\{w_i\}_0^{N_0}$. The norm of the initial residual is denoted by ρ^{-1}. By the construction, elaborated below, this quantity can be chosen arbitrarily small. One notes that Theorem 3.1 of [17] is a rigorous analytical result. This result may be used:

 (1) for *local* uniqueness;
 (2) for establishing continuity of the mapping N.

The critical step in the construction is the definition of the *approximate* right inverse of the derivative of F_w at each step. We note that the inverse used during the corrector/predictor step, denoted by H in [17], is required to satisfy a less stringent approximation of the identity condition than the inverse used for the predictor/corrector step, denoted by G. The algorithm is outlined now. One begins by determining the solution w_0 of Laplace's equation with specified boundary values w_{bdy}. This produces a zero residual, which permits a starting ρ^{-1} satisfying inequalities (2.16)–(2.17) of [17]. The Fréchet derivative of F is elementary when $\lambda = 0$, and simply reproduces the Laplacian part of F, independent of the calculated w_0. Homogeneous Dirichlet boundary conditions on the Dirichlet boundary Γ_D are required for the specification of the linearizations. Each of the approximate right inverses is denoted by the $\dagger$ notation. Initially, one defines: $[F_w(w_0, 0)]^\dagger := [F_w(\cdot, 0)]^{-1}$. After this obvious step, the algorithm requires definitions after both the Euler predictor and Newton corrector steps (cf. (3.7)–(3.8) of [17]). Thus, if the predictor v_k has been defined, one forms the residual $F(v_k, \lambda_k)$, *and* the approximate right inverse, via the first two terms of the virtual Neumann series for perturbations, as we now explain. For clarity, we suppress the second component (always zero) of the derivative mapping of F. Also, define the negative part g^- of a function g to be the minimum of g and zero so that $g^- \leqslant 0$. Set

$$\Gamma_k = [F_w(w_{k-1}, \lambda_{k-1}) + (\lambda_{k-1}[f_w(v_k) - f_w(w_{k-1})]^+ + \Delta\lambda[f_w(v_k)]^+)I]^\dagger.$$

Note that we have used the property that the approximate right inverses are invertible, and remain so under perturbation of F_w by positive multipliers of the identity. Inductively update the approximate right inverse by the formula:

$$[F_w(v_k, \lambda_k)]^\dagger = \Gamma_k - \Gamma_k[\lambda_{k-1}[f_w(v_k) - f_w(w_{k-1})]^- + \Delta\lambda[f_w(v_k)]^-]\Gamma_k. \tag{C.1}$$

This is the truncated virtual Neumann series. Now define w_k by the Newton step (the notation G is used for emphasis): $w_k = v_k - G(v_k, \lambda_k)F(v_k, \lambda_k)$. An even simpler construction is used to update from corrector to predictor (cf. (3.7) of [17]; the updated approximate inverse utilizes the actual inverse: $(-\delta^2\Delta + \lambda_k[f_w(w_k)]^+ I)^{-1}$. If X_0 denotes the Dirichlet zero trace functions in H^1, analysis shows that the operators G are bounded from X_0^* to X_0; at each stage a multiplier (not exceeding $\sqrt{1 + \gamma_k}$) of the preceding bound is introduced. One computes, for J the Riesz map in an equivalent norm: $\gamma_k = \|J\|^2\{\sup |[f_w(v_k) - f_w(w_{k-1})]^-| + \Delta\lambda|[f_w(v_k)]^-|\}^2$ in the predictor/corrector case. It is elementary that $\gamma_k \leqslant \gamma$, for a fixed positive constant γ. The hypotheses on the corrector/predictor map lead to a simple uniform bound in terms of the Laplacian. When restricted to L^2, the approximate inverse operators are positive definite, symmetric, and bounded. The maximum bound M_G for the family $\{G\}$ defined in this way does not exceed $\delta^{-2}\|(-\Delta)^{-1}\|$, multiplied by the product expansion factor above: $\sqrt{1 + \gamma}$. The approximation of the identity condition is now routine, as is the Lipschitz condition. At the completion of the homotopy, the approximate inverses are defined in a manner similar to (C.1), with $\Delta\lambda$ suppressed, and all iterates defined as correctors. The argument that M_G remains a valid bound for the inverse norms now requires an infinite product estimate based on the convergence estimate (2.18) of [17]:

$$c_0 = \prod_1^\infty (1 + \alpha_k) \leqslant \left(\frac{M_G}{\delta^2\|(-\Delta)^{-1}\|}\right)^2.$$

Here, α_k is bounded by $c\rho^{-1}2^{-k}$ for some constant c, as follows by estimating the terms $\|w_k - w_{k-1}\|^2_{X_0}$ via the analysis of [17]. The preceding discussion leads then to M_G as defined if ρ^{-1} satisfies $\exp(2c\rho^{-1}) < 1 + \gamma$. It follows that, at the termination of the predictor/corrector steps, one is in the domain of convergence of the approximate Newton method completely defined above. This permits the identification of a solution in an unambiguous manner. Continuity of N in L^2, required for the Schauder theorem, follows from the explicit definition of the approximate inverses via a formula analogous to (C.1).

References

[1] N.B. Abdallah, A. Unterreiter, On the stationary quantum drift-diffusion model, Z. Angew. Math. Phys. 49 (1998) 251–275.
[2] M. Ancona, G. Iafrate, Quantum correction to the equation of state of an electron gas in a semiconductor, Phys. Rev. B 39 (1989) 9536–9540.
[3] M. Ancona, H. Thiersten, Macroscopic physics of the silicon inversion layer, Phys. Rev. B 35 (1987) 580.
[4] M.G. Ancona, Z. Yu, R.W. Dutton, P.J.V. Vorde, M. Cao, D. Vook, Density-gradient analysis of MOS tunnelling, IEEE Trans. Electr. Devices 47 (12) (2000) 2310–2319.
[5] R.E. Bank, W.M. Coughran, L.C. Cowsar, Analysis of the finite volume Scharfetter–Gummel method for steady convection diffusion equations, Comput. Visualizat. Sci. 1 (3) (1998) 123–136.
[6] S. Carl, J. Jerome, Drift-diffusion in electrochemistry: thresholds for boundary flux and discontinuous optical generation, Applicable Anal. 83 (2004) 915–931.
[7] P. Ciarlet, The Finite Element Method for Elliptic Problems, North-Holland, Amsterdam–New York–Oxford, 1978.
[8] T.I. Consortium, International Technology Road Map for Semiconductors, Tech. Rep., ITRS Consortium (2005).
[9] S. Datta, Nanoscale device modeling: the Green's function method, Superlattices Microstruct. 28 (4) (2000) 253–278.
[10] C. de Falco, Quantum-corrected drift-diffusion models and numerical simulation of nanoscale semiconductor devices, Ph.D. Thesis, Università degli Studi di Milano, 2006.
[11] C. de Falco, A.L. Lacaita, E. Gatti, R. Sacco, Quantum-corrected drift-diffusion models for transport in semiconductor devices, J. Comput. Phys. 204 (2) (2005) 533–561.
[12] I. Ekeland, R. Temam, Convex Analysis and Variational Problems, North Holland and American Elsevier, 1976.
[13] E. Gatti, S. Micheletti, R. Sacco, A new Galerkin framework for the drift-diffusion equation in semiconductors, East West J. Numer. Math. 6 (2) (1998) 101–135.
[14] D. Gilbarg, N. Trudinger, Elliptic Partial Differential Equations of Second Order, Springer-Verlag, New York, 1977.
[15] H.K. Gummel, A self-consistent iterative scheme for one-dimensional steady-state transistor calculations, IEEE Trans. El. Dev. ED-11 (1964) 455–465.
[16] C. Jacoboni, P. Bordone, The Wigner-function approach to non-equilibrium electron transport, Rep. Prog. Phys. 67 (7) (2004) 1033–1071.

[17] J. Jerome, Approximate Newton methods and homotopy for stationary operator equations, Constr. Approx. 1 (1985) 271–285.
[18] J. Jerome, Consistency of semiconductor modeling: an existence/stability analysis for the stationary van Roosbroeck system, SIAM J. Appl. Math. 45 (1985) 565.
[19] J. Jerome, Analysis of Charge Transport, Springer-Verlag, New York, 1996.
[20] J.W. Jerome, T. Kerkhoven, A finite element approximation theory for the drift-diffusion semiconductor model, SIAM J. Numer. Anal. 28 (1991) 403–422.
[21] A. Jüngel, Quasi-hydrodynamic Semiconductor Equations, Progress in Nonlinear Differential Equations and Their Applications, Birkhäuser, 2001.
[22] A. Jüngel, A. Unterreiter, Discrete minimum and maximum principles for finite element approximations of non-monotone elliptic equations, Numerische Mathematik 99 (2005) 485–508.
[23] C. Jungermann, C. Nguyen, B. Neinhüs, S. Decker, B. Meinerzhagen, Improved modified local density approximation for modeling of size quantization in NMOSFETs, in: Technical Proceedings of the 2001 International Conference on Modeling and Simulation of Microsystems, 2001.
[24] M. Krasnosel'skii, Topological methods in the theory of non-linear integral equations, Pergamon Press, 1964.
[25] M. Krasnoselskii, G. Vainikko, P. Zabreiko, Y.B. Rititskii, V. Stetsenko, Approximate solution of operator equations, Wolters-Noordhoff, Groningen, 1972.
[26] S. Laux, A. Kumar, M. Fischetti, Ballistic FET modeling using QDAME: quantum device analysis by modal evaluation, IEEE Trans. Nanotechnol. 1 (4) (2002) 255–259.
[27] P. Markowich, The Stationary Semiconductor Device Equations, Springer-Verlag, Wien, 1986.
[28] P. Markowich, C. Ringhofer, C. Schmeiser, Semiconductor Equations, Springer-Verlag, Wien, 1990.
[29] F. Mehats, P. Degond, S. Gallego, An entropic quantum drift-diffusion model for electron transport in resonant tunneling diodes, J. Comput. Phys. 221 (2007) 226–249.
[30] F. Mehats, S. Gallego, Entropic discretization of a quantum drift-diffusion model, SIAM J. Numer. Anal. 43 (5) (2005) 1828–1849.
[31] R. Pinnau, A. Unterreiter, The stationary current–voltage characteristics of the quantum drift-diffusion model, SIAM J. Numer. Anal. 37 (1) (1999) 211–245.
[32] A. Pirovano, A. Lacaita, A. Spinelli, Two-dimensional quantum effects in nanoscale MOSFETs, IEEE Trans. Electron Devices 1 (47) (2002) 25–31.
[33] H.G. Roos, M. Stynes, L. Tobiska, Numerical Methods for Singularly Perturbed Differential Equations, Springer-Verlag, Berlin Heidelberg, 1996.
[34] D.L. Scharfetter, H.K. Gummel, Large signal analysis of a silicon read diode oscillator, IEEE Trans. Electron Devices (1969) 64–77.
[35] S. Selberherr, Analysis and Simulation of Semiconductor Devices, Springer-Verlag, Wien, 1984.
[36] H. Wong, Beyond the conventional transistor, IBM J. Res. Dev. 46 (2/3) (2002) 133–168.